HIGH PERFORMANCE FIBER REINFORCED CONCRETE FOR THE SHEAR REINFORCEMENT: EXPERIMENTAL AND NUMERICAL RESEARCH

F. Soltanzadeh[*1], J. A. O. Barros[1], R. F. C. Santos[2]

[1]ISISE, Dep. Civil Eng., School Eng., University of Minho, Campus de Azurém 4800-058 Guimarães, Portugal

[2]IPT- Instituto de Pesquisas Tecnologicas, Civil Engineer, Center for Infrastructure construction technology, 05508-901 Sao Paulo, SP, Brazil.

ABSTRACT

High performance fiber reinforced concrete (HPFRC) is developing rapidly to a modern structural material with unique rheological and mechanical characteristics. Despite applying several methodologies to achieve self-compacting requirements, some doubts still remain regarding the most convenient strategy for developing a HPFRC. In the present study, an innovative mix design method is proposed for the development of high-performance concrete reinforced with a relatively high dosage of steel fibers. The material properties of the developed concrete are assessed, and the concrete structural behavior is characterized under compressive, flexural and shear loading. This study better clarifies the significant contribution of fibers for shear resistance of concrete elements.

This paper further discusses a FEM-based simulation, aiming to address the possibility of calibrating the constitutive model parameters related to fracture modes I and II.

Keywords: High performance fiber reinforced concrete; Mechanical properties; Shear reinforcement; Image Analysis; Finite element simulations

- [*]Author to whom the correspondence should be sent (f.soltanzadeh@civil.uminho.pt).
-

1. INTRODUCTION

In late twentieth century, self-compacting concrete (SCC) capable of flowing along the framework, passing through reinforcements and filling voids and corners under its self-weight has been developed with the objective of simplifying the casting operation of large concrete elements with complex geometries and/or a high percentage of reinforcements. This technology was first developed using a simple mixture proportioning system and exhibited further advantages in the improvement of the precast industry, producing thinner and lighter elements and economizing time and costs. According to the primary method of concrete proportioning, the amounts of coarse and fine aggregates were kept constant so that self-compatibility was achieved easily by adjusting the water/cement ratio [1]. Since then, various investigations have been carried out to obtain a rational mix design method for tailoring SCC with higher rheological and mechanical performance. Additionally, a wide range of admixtures and fillers were introduced to SCC, including applying fine particles and reducing the free water content, which has contributed to tailor the cohesion and viscosity requisites, thus improving the stability of SCC [2]. In fact, by using fine fillers, such as silica fume and fly ash, the voids between cement particles are filled, causing a very dense and compact cement matrix. The use superplasticizers was another alternative for providing the required flowability and self-compacting ability of the mix with lower water contents [3]. By combining SCC with discrete steel fibers the SCC post-cracking tensile strength and energy absorption capacity was increased [4]. However, there still remain some questions about the most appropriate methodology for tailoring an optimum SCC composition when a relatively high content of fibers is used for the reinforcement of this material in order to achieve a fiber reinforced concrete with high post-cracking residual strength and flowability, herein designated as high-performance fiber-reinforced concrete (HPFRC). Thus, in the present study, a mix design method is proposed to develop HPFRC by means of defining the proportions of constituent materials of the binder paste, as well as a granular skeleton in an optimum manner. The developed HPFRC presents clear advantages in terms of structural performance compared to conventional concrete. The HPFRC was developed in order to have aimed properties in its fresh and hardened stages, namely a suitable flowability to be poured without vibration and attain a relatively high compressive strength at early age, in line with precast prestressed concrete element production demands.

In general, the use of steel fibers (SF) in concrete technology as a reinforcement system improves the behavior of cement-based materials, mainly in the post-cracking stage. The reinforcement effectiveness of SF depends on the matrix properties, fiber type and content, application technology of the fiber concrete, and geometry of the element to be produced [5-7]. Concrete shear behavior is reported as one of the most significant enhancements achieved by adding fibers to the concrete matrix [8, 9]. The experimental evidences confirmed the efficiency of fibers as shear reinforcement to enhance the ultimate shear capacity and ductility of the structural elements [10, 11]. The steel fibers increase the bearing capacity of the concrete elements and, therefore, bring the member up to yielding of rebars [12]. The advantages associated with the addition of steel fibers to a concrete mix can also be investigated under pure shear loading at the material level, where the pure shear loading is defined in literature as a loading condition in which a specimen is subjected to equal and opposite parallel forces with negligible bending [13]. However, there is no unanimous idea about the existence of shear failure in concrete because the crack is assumed to be developed normal to the principal tensile stress direction and causes the damage initiation and propagation of concrete element under the fracture mode I [14]. Nevertheless, in cases where the shear stress zone is narrow enough, for instance, in the case of push off specimens, the existence of mode II failure is evident [9]. Thus, the present study attempts to characterize the shear behavior of the developed HPFRC by means of an innovative specimen capable of concentrating the shear stress along its narrow shear ligaments. The results obtained from this part of the study indicate that the application of steel fibers, which limits the opening of the tensile cracks, causes shear-dominated failure with considerable ductility. Due to the pullout resistance and dowel action of fibers, a relatively high residual load carrying capacity is obtained in this type of tests.

The effect of fiber orientation on HPFRC fracture behavior is another aspect that is taken into consideration by means of image analysis. It is observed that the level of improvement of the concrete behavior by using fibers is sensitive to fiber dispersion and orientation. The later property of a fiber reinforced concrete is a crucial aspect, which represents the possibility of application the steel fibers as an alternative to the conventional reinforcement in the constructions [15]. In general, factors such as the fiber length and volume fraction, wall effects generated by the geometry of the formwork of the element to be cast, and the interactions between fibers and aggregates during mixing and casting influence the orientation and dispersion of the fibers inside the matrix. The flowability of concrete has a significant impact in this context, due to the fiber perturbation effect, especially when using relatively long fibers or a high fiber volume fraction. The steel fibers do not easily disperse in a concrete mix, due to its stiff nature. Thus an optimized SCC can be achieved only by considering the material property, geometry and content aspects of the fibers [3]. Through the balanced performance and the adequate viscosity of the HPFRC proposed in the present study, the fibers were found to be well orientated along the casting-flow direction. They enhanced the ductility and improved the post-cracking energy absorption capacity and toughness by effectively offering resistance to the propagation of microcracks [16].

After characterizing experimentally the shear behavior of HPFRC, the applicability of a multi-directional fixed smeared crack constitutive model [17] on the simulation of the shear behavior registered in the experimental tests was appraised. To obtain the fracture mode I parameters of the developed HPFRC, an inverse analysis [3] was carried out using the experimental results obtained from the three point bending tests on HPFRC notched beams.

2. MIX DESIGN METHOD

In the present study, the methodology to formulate a HPFRC mix design is based on the following three phases: (i) definition of the proportion of constituent materials for developing an optimized paste; (ii) determination of the optimum volume percentage of each type of aggregates in the granular skeleton of the concrete; and (iii) assessment of an optimum correlation between the paste and the solid skeleton in order to obtain HPFRC that meets the requirements of SCC, together with the satisfied mechanical performance in the harden stage in accordance with the demands of the project.

The applied materials for tailoring the mix were cement, CEM I 42.5R, fly ash class F, limestone filler, superplasticizer, water, three types of aggregates (containing fine and coarse river sand, and crushed granite) and hooked end steel fiber of 35 mm in length, an aspect ratio of 64 and a yield stress of 1100 MPa.

In the following section, the procedure for obtaining the optimum dosage of each material is described in detail.

2.1 Optimum Binder Paste Composition

In the first phase of the study, the optimum dosage of superplasticizer, fly ash, limestone filler and cement, as well as the water-to-binder ratio (w/b), were obtained using Marsh cone and mini-slump tests.

Since the physical properties of cement, fly ash and limestone filler influence the rheological behavior of fresh concrete, the properties of the adopted fine materials were tested and summarized on Table 1. The shape and size of cement particles influence the rate of hydration. These characteristics of cement also affect the packing density of the paste, and consequently increase the amount of free water available to increase the workability of the mixture. Application of the limestone filler, which occupies the voids between the cement particles due to the finer size compared to the cement, improves concrete durability [18, 19]. Also, the spherical-shape particles of the fly ash, which act as micro-rollers, significantly decrease the friction and the flow resistance of the paste.

2.1.1 Selection of the suitable superplasticizer

Since the use of a suitable superplasticizer is fundamental for guaranteeing SCC requirements, a series of pastes composed of cement, water and several types and dosages of superplasticizer (Glenium (BASF): SKY 617, 77 SCC, ACE 426 and SKY 602, respectively, named as SP1 to SP4 in the present research) were tested to find the most effective superplasticizer on the flowability and viscosity of the paste. All superplasticizers were based on polycarboxylic ether (PCE) polymers with high dispersing power, workability retention and fast strength development.

The pastes were prepared using a constant water-to-cement ratio (w/c) of 0.35 to have a good flowability without bleeding. Fig. 1a defines the relationship between the logarithm of the marsh flow time versus the percentage of superplasticizer. By increasing the volume percentage of superplasticizer in the paste, the marsh flow time is reduced up to the "saturation point", after which an increase in the dosage of the superplasticizer does not change the flow time significantly. The saturated dosage of each superplasticizer in the prepared pastes is marked as an unfilled marker in Fig. 1a. Application of the superplasticizer in the saturated dosage makes the paste have the highest fluidity without bleeding or segregation [20]. Decreasing the mean flow time by increasing the dosage of superplasticizers appears to be well fitted by a polynomial curve, as shown in Fig. 1b.

Among all of the tested superplasticizers, two superplasticizers, one caused the highest flowability, named as SP4 in this research, and the other one led to obtain the highest viscosity of the pastes, SP1, at the saturation point, were selected in this study.

2.1.2 Determination of the optimum dosage of fly ash

A series of flow tests were carried out on binder pastes made of cement, which was replaced by various dosages of fly ash, water and a minimum dosage of the selected superplasticizers ("SP1" and "SP4"). The water content was defined as 88% of the fine materials volume, and the fly ash dosages were varied between 0 to 55% of the cement volume. During these tests, the spread diameter of the control past "D_{Cont}", which produced without application of fly ash, were compared with the spread diameter of the testing series of pastes "D_{test}", included of various dosages of fly ash, as shown in Fig.2. This figure that represents the influence of the cement replacement by fly ash on the relative spread (D_{test}/D_{Cont}), shows that the flowability can be improved rapidly by replacing up to 25% of the cement volume with fly ash. By replacing 25% to 35% of cement by fly ash the flowability in the paste containing superplasticizer SP4 has reduced, whereas an increase was registered when superplasticizer SP1 was used. Above 35% of cement replacement by fly ash has small influence on the flowability of the pastes.

The relative spread of the paste containing SP4 was always higher than of the paste including SP1. However, cement replacement by fly ash above 25% caused bleeding of the paste when using superplasticizer SP4, while this percentage can increase up to 35% if superplasticizer SP1 is adopted without evidence of this phenomenon. As a result, the rest of the research was carried out using superplasticizer SP1 and fly ash in contents of 30% and 35% of the cement volume.

2.1.3 Determination of the optimum dosage of limestone filler

The paste was optimized by taking the benefits of limestone powder with the pore filling effect in producing a more compacted concrete structure with better cohesiveness, mechanical strength and durability [21, 22]. To define the optimum dosage of limestone filler, the flow test series were performed on the paste compositions made of 30% or 35% fly ash and different percentages of limestone filler relative to the cement volume. All series of the pastes were produced using a minimum dosage of superplasticizer SP1 and the content of mixing water was 88% of the total fine materials volume.

Fig. 3 represents the relationship between the relative spread of the paste (D_{test}/D_{Cont}) and the dosage of limestone filler. The best percentage of limestone filler, which caused the maximum spread of the paste without observation of the paste bleeding, was chosen as 30%. Regardless to the paste bleeding by using higher doses of limestone filler, two additional amount of 35% and 50% limestone were considered to study the effect of the filler dosage on the compressive strength of the corresponding mortar. These dosages were further selected to investigate if the bleeding of the paste also occurs when the paste is combined with aggregates for producing the corresponding mortar. The three selected limestone percentages are shown with unfilled marks in Fig. 3. The process for determining the optimum dosage of limestone filler and fly ash was finalized after performing compressive tests on nine $50 \times 50 \times 50\,\mathrm{mm}^3$ cubic mortar specimens at the age of 7 days (in accordance with ASTM C 109 / C109M - 11b and BS EN 197-1 [23, 24]).

According to the results presented in Fig. 4, the decrease of activation energy when cement is replaced fly ash, mainly at early ages [25] justifies the higher compressive strength for the series of specimens made by lower dosage of fly ash [26, 27]. Since the strength gain of the mortar specimens at the early age is mostly resulted from hydration of the cement, application of higher replacement of cement by filers caused a reduction of compressive strength. Similar tendency was also reported by Pereira, 2006 [20]. For limestone filler in percentage between 30% and 50% the compressive strength for the specimens was not significantly affected for the series of 35% of fly ash. However, application of limestone filler higher than 30% of cement volume caused a pronounceable bleeding in both series of the composites. Thus for producing the paste, capable of presenting a good flowability and compressive strength, 30% of the cement volume was selected as the optimum dosage of fly ash and limestone filler in the final composition.

2.1.4 Determination of the optimum dosage of superplasticizer

The optimum dosage of the selected superplasticizer was obtained by testing the flowability of several paste compositions, including distinct dosages of superplasticizer, constant ratio of water to cement and fly ash binder materials weight (w/b) of 0.28, and the optimum content of the fine materials: cement, fly ash and limestone filler. The superplasticizer proportions were defined in terms of the weight percentage of the fine materials. Fig. 5 indicates the relative spread (D_{test}/D_{Cont}) and flow time of each paste sample versus dosages of superplasticizer. The optimum percentage of superplasticizer was 1.2% of the fine materials weight. A summary of the optimized paste composition is presented in Table 2.

2.2 Determination of the optimum Aggregate Proportion

The second phase of the HPFRC mix design is composed by the evaluation of the optimum grading of the concrete solid skeleton. Since the particles interact volumetrically and not by weight [28] the aggregate gradations were determined on the basis of the volume. In accordance with ASTM C 29 and BS EN 1097-3 [29, 30], the shoveling procedure was adopted to access the loose bulk density for three types of aggregates, whose properties are indicated in Table 3. In this phase it was assumed that 90 Kg/m^3 steel fibers will be used in the HPFRC, since preliminary bibliographic research has indicated to be a suitable fiber content for constituting a cost competitive shear reinforcement system for the total replacement of conventional stirrups in flexurally RC beams [31].

To make the most compact solid skeleton, the following procedure was carried out: first of all, the coarse aggregate and fibers were used to fill the measuring cylinder. Because the fibers were expected to settle between the stone particles, the volume of coarse aggregate was kept constant, equal to the volume of the cylinder, and the river sand was added gradually until no voids remained to be filled by river sand. In the last step, the fine sand was added to fill the smaller voids as much as possible. The test was stopped when no more fine sand was possible to add for the filling of voids. To reduce the voids in size and percentage in each stage of this process, its filling was made in three layers by shaking the measuring cylinder after charging each layer. Fig. 6 represents the influence of this skeleton organization process on its relative weight, where this last concept is the ratio between the final weight of solid composition obtained in the second and third steps to the weight of coarse aggregate and steel fibers mixture that was determined in the first step of test. It is verified that the relative weight has increased with the volume percentage of fine river sand and coarse river sand on the total aggregate composition. Table 4 presents the percentage of total volume of fine sand, river sand and coarse aggregate in the first obtained aggregate composition, named as “S1”.

In order to improve S1 aggregate composition until reaching the adequate flowability for SCC, an aggregate gradation method based on the Individual Percent Retained (IPR) curve (which presents the percentage of the combined aggregate retained on each sieve size), the one recommended by Minnesota DOT [28], was applied as the first trial. In this method, the minimum and maximum limits for the aggregate composition in normal concrete, which should be retained on different sieve sizes, are recommended in a graph (Fig. 7). By comparing S1 with the proposed upper and lower limits of this graph, it is clear that the proportion of some intermediate particles (1.18 mm to 2.36 mm) are lower (33 to 38%) than the minimum recommended limit, while the proportion of some coarse aggregates (19 mm to 4.75 mm) exceeds the recommended upper limit (21% to 85%). In order to improve S1 aggregate composition, an attempt was made to increase the gap-graded observed in this composition by increasing the volume of intermediate particles and reducing the coarser aggregates, considering the IPR curve limit lines. Thus a series of trial concrete mixes with different aggregate gradation and constant ratio of paste volume to total volume of concrete mix ($V_{paste} / V_{total} = 0.45$) were prepared to select the best aggregate composition in this context. The flowability of the concrete mixes made by two different aggregate compositions “S2” and “S3” and a constant dosage of optimized paste were evaluated by executing slump flow tests, whose results are presented in Table 4. It is observed that the lower the volume percentage of the coarse aggregates is, the higher is the flowability. However, to develop a relatively high compressive strength and cost competitive HPFRC, the reduction of the coarser aggregate should be limited. Among the tested aggregate compositions (S1 to S3), the last one (S3), including 37% of coarse aggregate and 63% of river sand (12% of fine and 51% of coarse), was found to increase the viscosity properly without segregation. Fig. 8 compares the grading of this optimal composition (S3) with the curves corresponding to the limits recommended by ASTM

C136. This figure shows that the solid skeleton of SCC includes higher percentage of finer particles compared to that of conventional concrete.

2.3 Concrete Proportioning

In the last phase of the HPFRC mix design, the content of paste in the concrete volume is evaluated. For this purposes several mixes were prepared with distinct paste/aggregate ratios to establish proper flowability in the final mix. The detailed procedure of mixing the compositions can be found elsewhere [18]. The flowability of each mix was evaluated by measuring the total spread diameter and the time to reach a spread diameter of 500 mm, T_{50}, in the slump test. The obtained results are presented in Table 5. In this study, the best paste/aggregate ratio was 0.48, which is called mix "B" in the table. No visual sign of segregation was detected in mix-B and the mixture presented good homogeneity and cohesion during flowing through the smaller orifice of the Abrams cone (during testing the flowability of the mix, the Abrams cone was always used in the inverted position). The mix reached the spread diameter of 500 mm in 3.5 sec, and a total spread diameter of 660 mm. Using a lower paste volume ratio was not able to assure good flowability in the mix (mix-A), while a higher paste volume (mix-C) has decreased both the compressive strength in about 28% and the homogeneity of HPFRC, since segregation was observed. The process adopted for tailoring HPFRC is summarized in the flowchart represented in Fig. 9.

3. MECHANICAL CHARACTERIZATION OF THE DESIGNED HPFRC

The mechanical performance of the developed HPFRC was evaluated based on the compressive, flexural, and shear behavior of hardened HPFRC 28 days specimens, with special focus on the flexural and shear performance due to the significant impact of fiber reinforcement in these mechanical properties.

3.1 Compressive and Flexural Behavior

To characterize the compressive behavior and elastic modulus of HPFRC, nine cylindrical specimens of 150 mm in diameter and 300 mm in height were cast without applying vibration. The tests were carried out in a servo-controlled equipment of 3000 kN maximum load carrying capacity by imposing a displacement rate of $5\ \mu m/s$ in the internal displacement transducer to control the test procedure.

The Young's modulus was obtained in accordance with the EN 12390-13 (2014) [32] recommendation, where three loading-unloading cycles were prescribed. Using three linear voltage displacement transducers, LVDTs, disposed at 120° around the specimen, the axial displacement of the specimens was monitored during the tests. The loading value was limited between an upper level of one-third of the compressive strength of the HPFRC and the lower level of 0.5 MPa. Finally the elastic modulus was computed as the ratio of the stress difference between loading and unloading cycles and the strain difference observed in the last unloading cycle.

Compressive strength of the cylindrical specimens was evaluated according to ASTM C39 / C39M - 14a [33]. The obtained results at three distinct ages of 3, 7 and 28 days are reported in Table 6. These results show that the strength and stiffness have increased rapidly with age, which suggests that the developed HPFRC is quite capable of being applied for constructing prefabricated elements. Taking the compressive strength value of HPFRC at 28 days as the reference, the influence of concrete age on the compressive behavior of the HPFRC was further estimated based on the modified expression recommended by Cunha et al. (2008b) [34] for predicting the compressive strength of steel fiber reinforced concrete (SFRC) at early ages. Fig. 10a compares the estimated compressive strength of the HPFRC with the experimental values. It is apparent that the analytical results are in good agreement with those obtained experimentally. Similar to the experimental results, the analytical approach predicts a rapid strength gain of concrete compressive strength at early ages, which might be associated with the optimum water content used for tailoring the concrete that reduced the macroscopic entrapped voids [35]. The high dosage limestone filler has also improved the bond between the paste and the aggregates, by reducing the wall effect in the transition zone between these two phases and, consequently, has improved the microstructure of the mix [22].

The average values of the elasticity modulus, obtained at each age, and the scatter of the corresponding results are illustrated in Fig. 10b. These results are in agreement with those estimated by using the equation proposed by Cunha et al. (2008b) [34] for the elasticity modulus of SFRC at early ages.

The flexural tensile behavior of the developed HPFRC was obtained by testing three simply supported notched beams with a $150 \times 150\ \mathrm{mm}^2$ cross section and 600 mm in length under three point loading conditions. The method of casting the specimens and curing procedures, position and dimensions of the notch sawn into the specimen, and specimen support conditions were those recommended by RILEM TC 162-TDF (2003) [36]. This type of test was carried out in close-loop displacement control by a displacement transducer installed at the midspan of the prismatic specimen. To avoid instability at the first phase of the crack formation and propagation, the displacement rate at midspan of the specimen was $1\,\mu$m/s up to the deflection of 0.1 mm, above which this rate was $3\,\mu$m/s. Fig. 11 shows the nominal flexural stress versus midspan deflection relationship of the specimens. From this relationship and by applying the equation proposed by RILEM TC 162 TDF (2003) [36] for converting the midspan deflection of the beam to crack mouth opening displacements (CMOD), the values of CMOD were calculated, the stress limit of proportionality $f_{fct,L}$ (considered the flexural stress up to a deflection of 0.05 mm) and the residual flexural tensile strength parameters, $f_{R,j}$ [N/mm^2], were determined. The obtained results are indicated in Table 7, and it is verified that up to a crack width of about 1.5 mm the flexural strength of the developed HPFRC has exceeded 15 MPa, and at 3.5 mm this composite still presents a flexural capacity of about 12 MPa.

3.2 Shear Behavior

3.2.1 Specimen preparations and test setup

ASTM or CSA organizations still have not proposed standard test methods to investigate the material properties of FRC under direct shear loading, such as shear strength and shear toughness [37]. In this context, some researchers have attempted to characterize the shear behavior of FRC using a push-off specimen. This specimen is made of two L-shaped blocks continuously connected by a notched surface through which the shear stress is transferred between both blocks, and the corresponding shear sliding is measured [38]. Although this specimen exhibited the possibility of measuring FRC properties under a direct shear load, the failure mechanism of the specimen appeared to be governed by splitting-tension rather than shear [9]. Thus, to characterize the shear behavior of HPFRC, in the present study, a new specimen is designed with some improvements over the push-off specimen. To evaluate the influence of fiber orientation and dispersion on the shear behavior of HPFRC, the designed specimen was extracted from different locations of prismatic elements of $150\times150\times600\,\mathrm{mm}^3$ dimensions. Since the shear specimens were extracted from different distances from the casting point selected in the preparation of the prismatic elements, the obtained results can also give some indications on the influence of the viscosity and flowability of the HPFRC on the shear behavior of this material. The shear specimens were categorized in four groups according to their location along the prismatic element, as shown in Fig. 12a. In this figure, the label “DSS x-y” is used to distinguish the specimens, where “x” represents the number of the group and “y” identifies the row number where the shear specimen was located in the prism.

Fig. 12b illustrates a schematic representation of the adopted double shear specimen (DSS). In accordance with this configuration, a rectangular specimen of $150{\times}146\,\mathrm{mm}^2$ cross-section and 47 mm thick was used to determine the response of HPFRC under direct shear loading. To localize the shear crack along the pre-defined shear planes, two notches of 25 mm depth and 5 mm width were executed at the top and bottom edges of the specimens. After performing preliminary shear tests on specimens with different shear plane dimensions [39], a shear plane area of $20{\times}100\,\mathrm{mm}^2$ was found to be appropriate for designing the DSS, which was assured by executing another notch, in the front and rear faces of the specimen, with a depth and a width of 13.5 mm and 5 mm, respectively. The selection of the orientation of the notched planes in the DSS specimen (orthogonal to the axis of the prismatic element) was governed by the purpose of providing results in terms of HPFRC shear behavior representative of the shear capacity of the corresponding prismatic element. By having DSS specimens with shear planes at different position along the axis of the prismatic element, as well as at different distance from the lateral faces of this element, the results from the DSS tests, complemented with the image analysis to determine the fiber orientation and distribution, can constitute a relevant information to extract conclusions on the influence of the rheological properties of the developed HPFRC, casting methodology and mold geometry on the shear behavior of this material.

To avoid the formation of flexural cracks in the outer lateral faces of the DSS specimens, one carbon fiber reinforced polymer (CFRP) laminate was applied in each of these faces according to the near surface mounted technique [40], as represented in Fig. 12b.

The shear test setup was prepared in order to provide the load versus slip relationship in the notched planes, as well as the crack width during the loading process. For this purpose vertical and horizontal LVDTs were positioned according to the representation indicated in Fig. 12b. The extremities of the aluminum Z shape plates supporting the horizontal LVDTs were bonded to the lateral faces of the vertical notches in order to measure exclusively the crack width of these notches. The specimen was supported on two rigid edges, 61 mm in distance, and was loaded by means of two loading points, as depicted in Fig. 12b. This loading condition produced a predominant shear stress zone along the ligaments of the specimen, but bending stresses are not possible to completely exclude in this zone due to the arm formed by the action and reaction loads. The tests were executed in a servo-controlled testing machine of a bearing capacity of 150 kN, conducted under displacement control at a rate of $1\,\mu$m/s by using an external displacement transducer that measured the vertical deformation of the specimen. During the tests, one LVDT recorded the vertical displacement, while three others monitored the crack openings along the ligaments on each side of the DSS (Fig. 12b).

3.2.2 Results and discussion

During the loading process of the specimens, several small diagonal cracks developed along the ligaments of the DSS. These cracks joined together and formed a crack band along the shear plane, as presented in Fig. 13. During the formation and propagation of the smeared shear cracks, the fibers that bridge these cracks offer resistance to this cracking process due to the fiber reinforcement mechanisms detailed elsewhere [41]. Due to the beam type nature of the prismatic element, fibers have a tendency to be oriented along the axis of the prism and parallel to the main horizontal plane of the prism. Since the smeared shear cracks have an average inclination of 63 degrees (Fig. 13a), and are separated by micro-struts in compression, the fiber pullout reinforcement mechanisms of the fibers bridging these cracks (with average inclination angle of 42°) are not only benefited of the inclination of the fiber in relation to the crack shear planes [42], but also from the lateral confinement provided by the indicated inclined concrete compressive micro-struts (represented by C-C arrows in Fig. 13a).

The results obtained in terms of the load versus slip (P-s) and load versus CMOD (P-w) are presented in Fig. 14. Up to crack initiation, which occurs for a load level of about 20 kN that is almost 1/3 of the average peak load, the very small values of the opening and the sliding only represent the axial and shear elastic deformation of the concrete volume of the notch. Between cracking load and peak load the P-s and P-w have a pronounced nonlinear variation due to the post-cracking softening nature of the concrete and reinforcement mechanisms of fibers bridging the cracks. The smooth load decay after peak load is controlled by the fiber reinforcement mechanisms. In fact, the fibers offer resistance to the crack opening and sliding (micro dowel-effect), which delays the loss of shear contribution due to the aggregate interlock. This justifies the relatively high shear capacity of HPFRC at specimen scale, $\tau_{\max} = p_{\max} / (2b_{eff} . d_{eff}) = 14.5\,\text{MPa}$, where $\tau_{\max}$ is the average shear strength, $p_{\max}$ is the average peak load supported by the DSS specimen, and b_{eff} = 20 mm and d_{eff} = 100 mm are the effective width and depth of the specimen (Fig. 12b), respectively.

The average peak load was attained at an average slip of 1.6 mm and an average crack width of 1.2 mm. This means that the shear sliding of the notched plane has widen more than sliding, due to the favorable combined effect of micro-dowel mechanism of the fibers bridging the shear cracks and shear resistance of the micro compressive struts that restrict the shear sliding. Furthermore, the occurrence of micro-spalling of matrix around the fibers at the shear plane during the fiber pullout process, due to fiber snubbing effect, promotes the predominance of crack width over crack sliding [43].

Fig. 14a compares the relationship between the average load and slip, for the specimens located along the 3 rows and in 4 groups that were extracted from the HPFRC prism (Fig. 12a). Since the specimens from the middle row (row 2) were placed at a higher distance from the lateral walls of the mold, the fiber orientation due to wall effect is expected to be less pronounced resulting a fiber orientation closest to an isotropic nature. Due to the higher probability of having fibers better oriented in terms of being more effective for arresting the propagation and sliding of the shear cracks in these DSS specimens (Fig. 13a), it was expected a higher shear strength and post peak residual shear resistance when compared to the results of the specimens of rows 1 and 3. However, the small differences obtained experimentally (Fig. 14a) indicate that fiber distribution and orientation was not too different among all the specimens due to the good equilibrium of flowability and viscosity of the developed HPFRC. Similarly, the comparison of the average results of load-slip relationship of the specimens of the 4 groups demonstrates the proper rheology of the HPFRC since the small differences on the behavior of specimens located at different distance from the casting point indicate an homogeneous character of fiber distribution and orientation along the prism, a topic that will be further discussed in the following session.

3.2.3 Evaluation of the fiber distribution and orientation

The mechanical properties of the HPFRC were further analyzed by considering the fiber distribution and orientation parameters determined by image analysis technique applied to the tested specimens [44]. The images were captured from the shear plane of the specimens through which the shear cracks have propagated, as shown in Fig. 15. The adopted procedure for detecting the location and orientation of the fibers in this method is detailed in Soltanzadeh et al. (2012b) and Cunha et al. (2010) [39 and 42].

Using the image analyzing method, the fiber density “ N_f ” in the shear plane (i.e., the ratio between the total number of detected fibers “ N_f^T ”and the area of this plane “ A_f ”, $N_f = N_f^T / A_f$) was calculated. The fiber density of each specimen, as well as the average fiber density in each group of specimens is depicted in Fig. 16. The results evidence a marginal variation (11.5%) of fiber distribution along the prismatic element out of which the specimens were sawn. The figure demonstrates the proper balance of flowability and viscosity of the developed concrete that effectively caused the homogeneous distribution of fibers, as the DSS tests have already indicated.

Fig. 17 illustrates the relationship between the average shear toughness "W_{Fs}" per shear plane of the specimens and the average fiber density. According to Rao and Rao (2009) [16], the W_{Fs} represents the area under the shear load–slip curve until a slip corresponding to a certain CMOD. In Fig. 17 the W_{Fs} per shear plane is represented for CMOD of 0.1 to 0.4 mm. The direct relation between the shear toughness of the specimens and the fiber density, which is illustrated in this figure, expresses the significant influence of the fiber reinforcement on the shear toughness of the specimens. The favorable influence of the fiber density on the shear toughness occurred for the considered levels of CMOD, and has even a tendency to increase with the CMOD since the shear resisting mechanism due to aggregate interlock decreases with the increase of crack width and, therefore, the fiber reinforcement mechanisms have a predominant effect on the shear resistance.

The fiber orientation was the other property assessed from the image analysis, by determining the fiber orientation factor "η_θ". This factor was calculated as the average of the orientation of the fibers detected in the shear plane, and is obtained from the following equation:

$$\eta_\theta = \frac{1}{N_f^T} \cdot \sum_{i=1}^{N_f^T} \cos\theta_i \qquad (1)$$

where θ_i is the angle between the longitudinal axis of the ith fiber and a vector orthogonal to the shear plane, called the "out-of-plane angle". From this equation, it can be deduced that as the out-of-plane angle tends to zero degrees, the η_θ tends to the unit value, representing the limit situation of all the fibers orthogonal the crack plane.

Fig. 18a presents the relationship between the obtained values for the fiber orientation factor and the shear toughness of the tested specimens. In this figure it is represented the shear toughness for a CMOD of 0.2, 0.4 and 1 mm. It is verified a tendency for the increase of the shear toughness with the fiber orientation factor. The effect of fiber orientation factor seems to have an influence on the shear toughness of HPFRC similar to the fiber density. In fact it plays the complementary role for improving the shear toughness of the specimens. For instance, the shear toughness of the specimens DSS-1-3 and DSS-3-3 (Fig. 12a), which were extracted from the same row of the prismatic element, are compared in Fig. 18b. Although a higher fiber density was detected in the shear plane of DSS-1-3, it exhibited lower toughness up to a CMOD of about 0.35 mm. The activated fibers when the average CMOD was less than 0.2 mm are located in the area marked in red, where the number of fibers with elliptical cross section was higher in DSS-1-3. According to the adopted method for determining the fiber orientation [42], as different are the axis of this ellipse (cross section shape of the cut fiber) as higher is the inclination of the fiber), which means that these fibers were not so effective as a reinforcement system for small crack widths that justifies the smaller shear toughness of DSS_1_3 during this stage of loading. However, since DSS_1_3 has higher number of better oriented fibers in the central zone of the notched plane (signalized with green line), a higher gradient of shear toughness with CMOD was registered in this specimen, resulting similar values of this property at the final loading stage of both specimens. Therefore, the fiber reinforcement efficiency is the result of both fiber distribution and orientation in regard to the crack orientation.

4. FEM BASED SIMULATIONS

4.1 Numerical Model

This part of study is dedicated to FEM-based simulations in order to explore the possibilities of a smeared crack model for capturing the relevant features of the HPFRC DSS tests. This multi-directional fixed smeared crack model includes different approaches for modeling the cracked concrete shear behavior, and it is described in detail elsewhere [17], therefore in the present work only a short resume of this model is given.

The description of the formulation of the multi-directional fixed smeared crack model is restricted to the case of cracked concrete, at the domain of an integration point (IP) of a plane stress finite element. According to the adopted mode, stress and strain are related by the following equation

$$\Delta\underline{\sigma} = \underline{D}^{crco}\,\Delta\underline{\varepsilon} \qquad (2)$$

where $\Delta\underline{\sigma} = \{\Delta\sigma_1, \Delta\sigma_2, \Delta\tau_{12}\}^T$ and $\Delta\underline{\varepsilon} = \{\Delta\varepsilon_1, \Delta\varepsilon_2, \Delta\gamma_{12}\}^T$ are the vectors of the incremental stress and incremental strain components.

Due to the decomposition of the total strain into an elastic concrete part and a crack part, $\Delta\underline{\varepsilon} = \Delta\underline{\varepsilon}^{co} + \Delta\underline{\varepsilon}^{cr}$, in equation (2) the cracked concrete constitutive matrix, $\underline{D}^{crco}$, is obtained with the following equation [45]:

$$\underline{D}^{crco} = \underline{D}^{co} - \underline{D}^{co}\left[\underline{T}^{cr}\right]^T \left(\underline{D}^{cr} + \underline{T}^{cr}\,\underline{D}^{co}\left[\underline{T}^{cr}\right]^T\right)^{-1} \underline{T}^{cr}\,\underline{D}^{co} \tag{3}$$

where $\underline{D}^{co}$ is the constitutive matrix of concrete that depends of the Young's modulus and the Poisson's ratio of concrete, $\underline{T}^{\mathrm{cr}}$ is the matrix that transforms the stress components from the coordinate system of the finite element to the local crack coordinate system, and $\underline{D}^{cr}$ is a matrix that includes the constitutive law of the cracks installed in the IP. The constitutive law of a i$^{\text{th}}$ crack has two components:

$$\underline{D}_i^{cr} = \begin{bmatrix} D_n^{cr} & 0 \\ 0 & D_t^{cr} \end{bmatrix}_i \tag{4}$$

where $D_{n,i}^{cr}$ and $D_{t,i}^{cr}$ represent, respectively, the modulus correspondent to the fracture mode I (normal) and fracture mode II (shear) of the i^{th} crack. The crack opening propagation is simulated with the quadrilinear diagram represented in Figure 19a, which is defined by the normalized stress, α_i, and strain, ξ_i, parameters that define the transition points between the linear segments of this diagram, where G_f^I, f_{ct} are the fracture energy and the tensile strength of the concrete, while l_b is the crack band width that assures the results of the numerical simulations with a smeared crack approach are not dependent of the refinement of the finite element mesh [3].

To simulate the fracture mode II modulus, D_t^{cr}, a shear retention factor is currently used [45]:

$$D_t^{cr} = \frac{\beta}{1-\beta} G_c \tag{5}$$

where G_c is the concrete elastic shear modulus and β is the shear retention factor. The parameter β is defined as a constant value or as a function of the current crack normal strain, ε_n^{cr}, and of the ultimate crack normal strain, $\varepsilon_{n.u}^{cr}$, as follows,

$$\beta = \left(1 - \frac{\varepsilon_n^{cr}}{\varepsilon_{n,u}^{cr}}\right)^p \tag{6}$$

The present model also includes a softening crack shear stress *vs.* crack shear strain relationship, whose diagram is represented in Fig. 19b. The crack shear stress increases linearly until the crack shear strength is reached, $\tau_{t.p}^{cr}$, followed by a decrease in the shear residual strength (softening branch). This diagram is defined by the following equations:

$$\tau_t^{cr}(\gamma_t^{cr}) = \begin{cases} D_{t,1}^{cr}\,\gamma_t^{cr} & 0<\gamma_t^{cr}\leq\gamma_{t,p}^{cr} \\ \tau_{t,p}^{cr}-\dfrac{\tau_{t,p}^{cr}}{(\gamma_{t,u}^{cr}-\gamma_{t,p}^{cr})}(\gamma_t^{cr}-\gamma_{t,p}^{cr}) & \gamma_{t,p}^{cr}<\gamma_t^{cr}\leq\gamma_{t,u}^{cr} \\ 0 & \gamma_t^{cr}>\gamma_{t,u}^{cr} \end{cases} \tag{7}$$

The initial shear fracture modulus, $D_{t,1}^{cr}$, is defined by equation (5) by assuming for β a constant value in the range]0,1[. The peak crack shear strain, $\gamma_{t,p}^{cr}$, is obtained $\tau_{t,p}^{cr}$ from:

$$\gamma_{t,p}^{cr} = \frac{\tau_{t,p}^{cr}}{D_{t,1}^{cr}} \tag{8}$$

The ultimate crack shear strain, $\gamma_{t,u}^{cr}$, depends on the $\tau_{t,p}^{cr}$, shear fracture energy (mode II fracture energy), $G_f^{II} = G_{f,s}$, and l_b:

$$\gamma_{t,u}^{cr} = \frac{2G_{f,s}}{\tau_{t,p}^{cr}\, l_b} \tag{9}$$

In the present approach it is assumed that l_b is the same for both fracture mode I and mode II processes, but specific research should be done in this respect in order to assess the influence of these model parameters on the predictive performance of the behavior of elements failing in shear. In the present simulations the l_b was considered equal to the square root of the area of the IP. Five shear crack statuses are proposed and their meaning is schematically represented in Figure 19b.

The crack mode II modulus of the first linear branch of the diagram is defined by equation (5), while for the second linear softening branch it is obtained from:

$$D_{t,2}^{cr} = -\frac{\tau_{t,p}^{cr}}{\gamma_{t,u}^{cr}-\gamma_{t,p}^{cr}} \tag{10}$$

The crack shear modulus of the unloading and reloading branches is obtained from

$$D_{t,3,4}^{cr} = -\frac{\tau_{t,\max}^{cr}}{\gamma_{t,\max}^{cr}} \tag{11}$$

being $\gamma_{t,\max}^{cr}$ and $\tau_{t,\max}^{cr}$ the maximum crack shear strain already attained and the corresponding crack shear stress determined from the softening linear branch. Both components are stored to define the unloading/reloading branch (see Fig. 19b).

In free-sliding status ($\left|\gamma_t^{cr}\right| > \left|\gamma_{t,u}^{cr}\right|$) the crack shear modulus, $D_{t,5}^{cr}$, is null. To avoid numerical instabilities in the calculation of the stiffness matrix and in the calculation of the internal forces, when the crack shear status is free-sliding, a residual value is assigned to this term.

A free-sliding status is assigned to the shear crack status when $\varepsilon_n^{cr} > \varepsilon_{n,u}^{cr}$. The details about how the shear crack statuses were treated can be consulted elsewhere [17].

4.2 Assessment of the Mode I Crack Constitutive Law

The Mode I fracture parameters were assessed by means of an inverse analysis of the flexural test results obtained experimentally with the three point notched HPFRC beam bending tests presented in Section 3.1. This method is adopted in accordance with the previous studies of Barros et al. (2005) [46]. Since the fracture mode I propagation of hardened HPFRC was simulated by the quadrilinear stress-softening diagram represented in Fig. 19a, the inverse analysis procedure was followed by evaluating the parameters ξ_i, α_i (i=1 to 3), the tensile strength, f_{ct}, and the fracture energy, G_f^I, that minimize the ratio between the area underneath the experimental load-deflection curve and the numerical one.

The numerical curve was obtained by a FEM analysis, considering the specimen's geometry, and loading and support conditions in agreement with the experimental flexural test setup. Fig. 20 presents the simulated specimen, modeled by a mesh of four node plane stress finite elements with $2 \times 2\, IP$. To assure the formation of a single crack line along the specimen symmetry axis, the Gauss-Legendre integration scheme of $2 \times 1\, IP$ was adopted for the elements located in the notched area. Apart the elements located above the notch, where the elastic cracked behavior in tension was assumed, a linear elastic material behavior was assigned to all of the elements. The parameters ξ_i, α_i, f_{ct}, G_f^I, E, obtained from this inverse analysis are presented in Table 8, and the corresponding numerical force-deflection is compared to the corresponding experimental results in Fig. 11, where it is verified that a good agreement was obtained between the experimental and numerical load-deflection curves.

4.3 Simulation of the HPFRC Shear Behavior

The experimental shear tests with HPFRC DSS specimens were simulated numerically by using the model briefly described in session 4.1, and using for the fracture mode I parameters the values determined by inverse analysis, presented in Table 8. An FEM mesh composed of 430 plane stress elements of 4 nodes was generated in order to simulate the specimen, as shown in Fig. 21. A Gauss-point integration scheme of $2 \times 2\, IP$ was used in all of the elements, excluding the elements along the notched ligament, where $1 \times 2\, IP$ was used. The elastic-cracked material behavior was defined for the finite elements located along the shear ligament, while the others finite elements were assigned with an elastic type of material behavior. Due to the structural symmetry of the specimen, only half of the DSS was simulated.

Fig. 22 compares the load-slip and load-CMOD relationships obtained from the numerical simulations and experimental tests. When the conventional shear retention factor was used (considering any type of p parameter in Eq. (6)), it was verified that the model did not match the experimental results, and good agreement was found only at the initial part of the curves. By using a shear softening law, characterized by the fracture mode II parameters, the model was capable of capturing the behavior of HPFRC subjected to direct shear loading with a good estimation of the peak load as well as the structural softening behavior, mainly in terms of sliding, since the stress decay predicted numerically in the CMOD softening stage was not so pronounced as recorded experimentally. The inverse analysis process executed with the simulations of these experimental tests has allowed the determination of the fracture mode II parameters that define the crack shear stress shear versus crack shear strain diagram adopted in the present model (Fig. 19b), and the following results were obtained: β =0.001, $\tau_{t,p}^{cr}$ = 7.7 MPa, and $G_{f,s}$ = 6.5 N/mm. It is also noted that the obtained value of $t_{t,p}^{cr}$ represents the shear strength at the level of crack, while $\tau_{\max}$ =14.5 MPa, which is registered experimentally, represents the average shear strength of the specimen.

5. CONCLUSIONS

In the present study, an innovative method of designing was proposed to develop high performance fiber reinforced concrete (HPFRC) with rheological and mechanical properties suitable for the production of precast prestressed concrete elements (self-compacting character and relatively high compressive and post-cracking residual strength). Using this method, a total spread of 660 mm was obtained for the developed HPFRC composed of 90 Kg/m^3 of hooked end steel fibers. At 28 days the average compressive strength was about 68 MPa with a residual flexural tensile capacity up to a crack width of 1.5mm higher than 15 MPa.

The shear behavior of HPFRC was assessed by applying a shear loading configuration on a shear specimen designed for this purpose. From the obtained results the average shear strength of 14.5 MPa was obtained with a shear toughness of 15.3 kN.mm up to a CMOD of 0.3 mm (the maximum value allowed by CEB-FIP Model Code for accomplishing serviceability limit state conditions), revealing a high energy dissipation capacity in shear loading configuration. The shear strength was attained at an average slip of 0.18 mm, when the average crack opening was 0.15 mm, indicating the high effectiveness of the developed HPFRC in terms of shear capacity and stiffness, as well as in limiting the crack width up to its maximum shear capacity, which has favorable effects in terms of durability of this composite.

To assess the influence of fiber orientation and dispersion on the shear performance of HPFRC, image analysis was executed on the notched shear plane of the tested DSS specimens. It was verified that due to the good balance in terms of flowability and viscosity for the developed HPFRC, an almost homogeneous fiber distribution and orientation was assured

The material parameters of the fracture mode I were obtained by means of an inverse analysis applied to the force-deflection relationship recorded in the HPFRC notched beam bending tests, while the parameters of the fracture mode II were determined by executing an inverse analysis applied to the force-slip-CMOD registered in the DSS tests.

ACKNOWLEDGEMENTS

The research in this paper is part of the project "DURCOST - Innovation in reinforcing systems for sustainable pre-fabricated structures of higher durability and enhanced structural performance" with reference number of PTDC/ECM/105700/2008, supported by FCT. The authors also thank the collaboration of the following companies: Casais to manufacture the moulds, Ibermetais for supplying the steel fibres, Secil/Unibetão for providing the Cement, BASF for supplying the superplasticizers. The first author acknowledges the research grant in the ambit of this project.

REFERENCES

[1] H. Okamura, M. Ouchi, Self-compacting concrete development, present use and future, Proc. 1st International RILEM Symposium on Self-Compacting Concrete, Stockholm, Sweden, RILEM Publications S.A.R.L. 1999.

[2] B. Felekoğlu, S. Türkel, B. Baradan, Effect of water/cement ratio on the fresh and hardened properties of self-compacting concrete, Build. Environ. 42 (2007) 1795-1802.

[3] E.N.B. Pereira, J.A.O. Barros, A. Camões, Steel fiber reinforced self-compacting concrete: experimental research and numerical simulation, Structural Eng. 134 (2008) 1310-1321.

[4] A. Jansson, Fibres in reinforced concrete structures analysis, experiments and design, PhD thesis, Chalmers University of Technology, Göteborg, Sweden, 2008.

[5] F. Laranjeira, Design-oriented constitutive model for steel fiber reinforced concrete, PhD thesis, Polytechnic University of Catalonia, Barcelona, Spain, 2010.

[6] C. Cucchiara, L.L. Mendola, M. Papia, Effectiveness of stirrup and steel fibers as shear reinforcement, Cem. Concr. Compos. 26 (2004) 777-786.

[7] V.M.C.F. Cunha, Steel fibre reinforced self-compacting concrete, PhD Thesis, University of Minho, Guimarães, Portugal, 2010.

[8] E. Cuenca, P. Serna, P., (2013), Shear behavior of self-compacting concrete and fiber concrete push-off specimens, in K. H. Khayat, D. (Eds.), Design production and placement of self-consolidating concrete, Proceedings of SCC2010, RILEM Bookseries, Montreal, Canada, 1(2010) 429-466.

[9] B. Barragan, R. Gettu, L. Agullo, R. Zerbino, Shear failure of steel fiber-reinforced concrete based on push-off tests, ACI Mater. J. 103 (2006) 251-257.

[10] F.Minelli, A. Conforti, E. Cuenca, G.A. Plizzari, Are steel fibres able to mitigate or eliminate size effect in shear?, Mater. Struc. J. 47, (2014) 459-473. doi: 10.1617/s11527-013-0072-y.

[11] E.Cuenca, P. Serna, Failure modes and shear design of prestressed hollow core slabs made of fiber-reinforced concrete, Comp. Part B: Eng. J. 45 (2013) 952-964. ISSN 1359-8368, pp. 952-964, http://dx.doi.org/10.1016/j.compositeb.2012.06.005.

[12] E. Cuenca, P. Serna, Shear behavior of prestressed precast beams made of self-compacting fiber reinforced concrete, Const. Build. Mater. J. 45 (2013) 145-156. http://dx.doi.org/10.1016/j.conbuildmat.2013.03.096.

[13] M.R. Ayatollahi, M.R.M. Aliha, Cracked Brazilian disc specimen subjected to mode II deformation, Eng. Fracture Mechanics. 72 (2005) 493–503.

[14] M. Arrea, A.R. Ingraffea, Mixed mode crack propagation in mortar and concrete, Technical report, Cornell University, Ithaka, NY, 81-13 (1982).

[15] F. Laranjeira, S. Grünewald, J. Walraven, C. Blom, C. Molins, A. Aguado, Characterization of the orientation profile of steel fiber reinforced concrete, Mater. Struct. J. 44 (2011) 1093-1111.

[16] G.A. Rao, A.S. Rao, Toughness indices of steel fiber reinforced concrete under mode II loading, Mater. Struct. 42 (2009) 1173-1184.

[17] A. Ventura-Gouveia, Constitutive models for the material nonlinear analysis of concrete structures including time dependent effects, PhD Thesis, University of Minho, Guimarães, Portugal, 2011.

[18] F. Soltanzadeh, J.A.O. Barros, R.F.C. Santos, Steel fiber reinforced self-compacting concrete: from material to mechanical behavior, Technical report, University of Minho, Guimarães, Portugal, 12-DEC/E-19 (2012).

[19] E.N.B. Pereira, Steel fibre reinforced self-compacting concrete: from material to mechanical behaviour, Master Thesis, University of Minho, Guimarães, Portugal, 2006.

[20] P.C.C Gomes, Optimization and characterization of high-strength self-compacting concrete, PhD Thesis, Polytechnic University of Catalonia, Barcelona, Spain, 2002.

[21] M. Ghrici, S. Kenai, M. Said-Mansour, Mechanical properties and durability of mortar and concrete containing natural pozzolana and limestone blended cements, Cem. Concr. Comp. 29 (2007) 542-549.

[22] G.C. Isaia, A.L.G. Gastaldini, R. Moraes, Physical and pozzolanic action of mineral additions on the mechanical strength of high-performance concrete, Cem. Concr. Comp. 25 (2003) 69–76.

[23] ASTM C 109 / C109M - 11b, Standard test method for compressive strength of hydraulic cement mortars (using 2-in. or [50-mm] cube specimens), Annual Book of ASTM Standards, American Society of Testing Materials, 2011.

[24] BS EN 197-1, Cement – Part 1: Composition, specifications and conformity criteria for common cements, BSI, London, UK, 2000.

[25] M.A.D. Azenha, Numerical simulation of the structural behaviour of concrete since its early ages, PhD Thesis, University of Porto, Porto, Portugal, 2009.

[26] B. Felekoğlu, K. Tosun, B. Baradan, A. Altun, B. Uyulgan, The effect of fly ash and limestone fillers on the viscosity and compressive strength of self-compacting repair mortars, Cem. Concr. Res. 36 (2006) 1719-1726.

[27] G. Villain, V. Barogel-Bouny, C. Kounkou, Comparative study on the induced hydration, drying and deformations of self-compacting and ordinary mortars, Proc. 1st International RILEM Symposium, (1999) 131–142.

[28] D.N. Richardson, Aggregate gradation optimization- literature search, Technical report, University of Missouri- Rolla, Missouri , RDT 05-001(2005).

[29] ASTM C 29 / C29M – 09, Standard test method for bulk density ("unit weight") and voids in aggregate, Annual Book of ASTM Standards, American Society of Testing Materials, 2009.

[30] BS EN 1097-3, Tests for mechanical and physical properties of aggregates. Determination of loose bulk density and voids, British Standards Institution, 1998.

[31] F. Soltanzadeh, H. Mazaheripour, J.A.O. Barros, M. Taheri, J.M. Sena-Cruz, Experimental study on shear behavior of HPFRC beams reinforced by hybrid pre-stressed GFRP and steel bars", Proc. 7th International Conference on FRP Composites in Civil Engineering, CICE 2014, 2014.

[32] BS EN 12390-13, Testing hardened concrete - Part 13: Determination of secant modulus of elasticity in compression, 2014.

[33] ASTM C39 / C39M - 14a, Standard test method for compressive strength of cylindrical concrete specimens, Annual Book of ASTM Standards, American Society of Testing Materials, 2014.

[34] V.M.C.F. Cunha, J.A.O. Barros, J.M. Sena-Cruz, Modelling the influence of age of steel fibre reinforced self-compacting concrete on its compressive behavior, Mater. Struct. 41(2008) 465-478.

[35] P. Pereira, L. Evangelista, J. Brito, The effect of superplasticizers on the workability and compressive strength of concrete made with fine recycled concrete aggregates, Constr. Build. Mater. 28 (2012) 722-729.

[36] L. Vandewalle, RILEM TC 162-TDF, Test and design methods for steel fibre reinforced concrete σ-ε design method - Final Recommendation, Mater. Struct. 36 (2003) 560-567.

[37] A.A. Mirsayah, N. Banthia, Shear Strength of Steel Fiber-Reinforced Concrete, ACI Mater. J. 99 (2002) 473-479.

[38] F. Soltanzadeh, J.A.O. Barros, Test setup for the characterization of shear behavior of cement based materials, Technical report, University of Minho, Guimarães, Portugal, 11-DEC/E-23 (2011).

[39] F. Soltanzadeh, J.A.O. Barros, R.F.C. Santos, Study of the fracture behavior of fiber reinforced concrete under direct shear loading, Technical report, University of Minho, Guimarães, Portugal. 12-DEC/E-18 (2012).

[40] J.A.O. Barros, A.S. Fortes, Flexural strengthening of concrete beams with CFRP laminates bonded into slits, Cem. Concr. Compos. 27 (2005) 471-480.

[41] V.M.C.F. Cunha, J.A.O. Barros, J.M. Sena-Cruz, Bond-slip mechanisms of hooked-end steel fibers in self-compacting concrete, Materials Science Forum, Vols. 587-588 (2008) 877-881. http://www.scientific.net

[42] V.M.C.F. Cunha, J.A.O. Barros, J.M. Sena-Cruz, Pullout behaviour of steel fibres in self-compacting concrete, *Mater. in Civil Eng.* 22 (2010) 1-9.

[43] S.J. Foster, The application of steel-fibres as concrete reinforcement in Australia: from material to structure, Mater. Struct. 42 (2009). 1209–1220. DOI 10.1617/s11527-009-9542-7

[44] H.W. Reinhardt, C.U. Grosse, B. Weiler, Material characterization of steel fibre reinforced concrete using neutron CT, ultrasound and quantitative acoustic emission techniques, NDT and E International, No.5 (2001).

[45] J.M. Sena-Cruz, Strengthening of concrete structures with near-surface mounted CFRP laminate strips, PhD Thesis, University of Minho, Guimarães, Portugal, 2004.

[46] J.A.O. Barros, V.M.C.F. Cunha, A.F. Ribeiro, J.A.B. Antunes, Post-cracking behaviour of steel fibre reinforced concrete," Mater. Struct. 38 (2005) 47-56.

[47] ASTM C150 / C150M – 12, Standard specification for Portland cement, Annual Book of ASTM Standards, American Society of Testing Materials, 2012.

[48] BS EN 197-1, Cement. Composition, specifications and conformity criteria for common cements, 2012.

[49] ASTM C 618 – 12, Standard specification for coal fly ash and raw or Calcined natural Pozzolan for use in concrete, Annual Book of ASTM Standards, American Society of Testing Materials, 2012.

[50] BS EN 450-1, Fly ash for concrete. Definition, specifications and conformity criteria, 2012.

[51] ASTM C 127 – 12, Standard test method for density, relative density (specific gravity), and absorption of coarse aggregate, Annual Book of ASTM Standards, American Society of Testing Materials, 2012.

[52] BS EN 1097-6, Tests for mechanical and physical properties of aggregates. Determination of particle density and water absorption, 2000.

[53] ASTM C 128 – 12, Standard test method for density, relative density (specific gravity), and absorption of fine aggregate, Annual Book of ASTM Standards, American Society of Testing Materials, 2012.

[54] ASTM C 136 – 06, Standard test method for sieve analysis of fine and coarse aggregates, Annual Book of ASTM Standards, American Society of Testing Materials, 2006.

[55] BS 812-103.1, Testing aggregates. Method for determination of particle size distribution. Sieve tests, 1985.

A_f = shear plane area

$A_{F-u}^{\exp}$ = area below the experimental $F-u$ curves of three point bending test

A_{F-u}^{num} = area below the numerical $F-u$ curves of three point bending test

b = width of the specimen

b_{eff} = effective width of the DSS

$\underline{D}^{co}$ = linear elastic constitutive matrix

$\underline{D}^{cr}$ = crack constitutive matrix

$\underline{D}^{crco}$ = cracked material constitutive matrix

D_n^{cr} = fracture mode I modulus

D_t^{cr} = fracture mode II modulus

$\underline{D}_{I,i}^{cr}$ = the modulus correspondent to the fracture mode I of the i^{th} crack

$\underline{D}_{II,i}^{cr}$ = the modulus correspondent to the fracture mode II of the i^{th} crack

d_{eff} = effective depth of DSS

E = modulus of elasticity

F_j = load corresponding to $CMOD_j$

F_L = load at the limit of proportionality for three-point notched beams flexural tests

f_{ct} = concrete tensile strength

f_{ck} = characteristic value of compressive strength of concrete

f_{cm} = mean value of compressive strength of concrete

$f_{fct,L}$ = limit of proportionality

f_{Rj} = residual flexural tensile strength corresponding to $CMOD_j$ (j=1, 2, 3, 4)

G_c = elastic shear modulus

G_f^I = mode I fracture energy

G_f^{II} = mode II fracture energy

h_{sp} = distance between the tip of the notch and the top of the cross section

IP = integration point

L = span of the specimen

l_b = crack band width

N_f = fiber density

N_T^f = total number of fibers

P = load supported by the HPFRC DSS

$P_{\max}$ = average peak load supported by the HPFRC DSS

p_1 = shear degradation factor

s = slip value

T^{cr} = transformation matrix from crack local coordinate system to element local coordinate system

T_{50} = time to reach a spread diameter of 500 mm in the slump test

u = deflection

V_{paste} = volume of paste

V_{total} = total volume of concrete mix

w = width of cracks

W_{Fs} = shear toughness

α_i = normalized stress parameters (*i*=1, 2, 3)

β = shear retention factor

γ_t^{cr} = crack shear strain

$\gamma_{t,p}^{cr}$ = peak crack shear strain

$\gamma_{t,\max}^{cr}$ = maximum crack shear strain

$\gamma_{t,u}^{cr}$ = ultimate crack shear strain

$\Delta\underline{\sigma}$ = vectors of incremental stress components

$\Delta\underline{\varepsilon}^{cr}$ = crack strain vector

$\Delta\underline{\varepsilon}^{co}$ = elastic strain vector

$\Delta\underline{\varepsilon}$ = vectors of incremental strain components

δ_L = deflection at the limit of proportionality in three-point flexural tests

$\varepsilon_{n,u}^{cr}$ = ultimate crack normal strain

ε_n^{cr} = crack normal strain

ξ_i = normalized strain parameter (*i* =1, 2, 3)

η_θ = fiber orientation factor

θ_i = out-plane angle

μ = Poisson’s ratio

$\tau_{\max}$ = average shear strength

$\tau_{t,\max}^{cr}$ = maximum crack shear stress

$\tau_{t,p}^{cr}$ = shear strength at the level of the crack

Figure captions

Fig. 1 - (a) Marsh flow time at saturation point; and (b) flow time *vs.* dosage of superplasticizer

Fig. 2 - Relative spread of paste by replacing cement with different dosages of fly ash

Fig. 3 - Relative spread of paste made by different percentage of limestone filler

Fig. 4 - Compressive strength of mortar made of various percentages of limestone filler

Fig. 5 - Relative spread of the paste *vs.* the percentage of superplasticizer

Fig. 6 - Determination of the optimum composition of the solid skeleton

Fig. 7 - Comparison of the results with the limitation suggested by Minnesota DOT

Fig. 8 - Comparison of the results with the curves defining the upper and lower limits suggested by ASTM C136 for conventional concrete (fine aggregate includes the fine and coarse rive sand)

Fig. 9 - Flowchart of HPFRC mix design

Fig. 10 - Evolution with age of: (a) average compressive strength, and (b) average elasticity modulus

Fig. 11 - Nominal flexural stress-midspan deflection relationship

Fig. 12 - (a) Location of the specimens along the prismatic element (Top view); and (b) geometry and loading configuration of DSS specimen (dimensions in mm)

Fig. 13 - (a) Shear transfer during the initiation of the inclined cracks (b) formation of the crack band along the shear plane; and (c) fractured plane of the specimen

Fig. 14 - Experimental results of (a) load-slip; and (b) load *vs.* CMOD relationship

Fig. 15 - Sawn section of DSS for image analysis (dimensions in mm)

Fig. 16 - Fiber density along the beam length

Fig. 17 - Fiber density *vs.* shear toughness of the specimens

Fig. 18 - (a) Fiber orientation factor *vs.* shear toughness of the specimens; and (b) Comparison of two shear plane

Fig. 19 - Diagrams for modeling the (a) fracture mode I ($\sigma_{n,2}^{cr} = \alpha_1 \ f_{ct}$, $\sigma_{n,3}^{cr} = \alpha_2 \ f_{ct}$,

$\sigma_{n,4}^{cr} = \alpha_3 \, f_{ct}$, $\varepsilon_{n,2}^{cr} = \xi_1 \, \varepsilon_{n,u}^{cr}$, $\varepsilon_{n,3}^{cr} = \xi_2 \, \varepsilon_{n,u}^{cr}$, $\varepsilon_{n,4}^{cr} = \xi_3 \, \varepsilon_{n,u}^{cr}$); and (b) fracture mode II at the crack coordinate system

Fig. 20 - Finite element mesh relevant characteristic, load and support conditions of the type of specimen adopted in the inverse analysis

Fig. 21 - Finite element model for simulating mixed mode fracture tests

Fig. 22 - Comparison between numerical and experimental results of (a) load *vs.* slip; and (b) load *vs.* CMOD relationships

Table captions

Table 1-	Physical property of cement, fly ash and limestone filler
Table 2-	Optimum paste composition
Table 3-	Aggregate properties
Table 4-	Aggregate compositions and their effects on flowability of a concrete mix
Table 5-	Concrete compositions executed with different paste percentages
Table 6-	Compressive strength and Young's modulus of HPFRC
Table 7-	Average limit of proportionality and residual flexural tensile strength parameters of HPFRC beams
Table 8-	Values of the fracture parameters defining the stress-strain softening laws

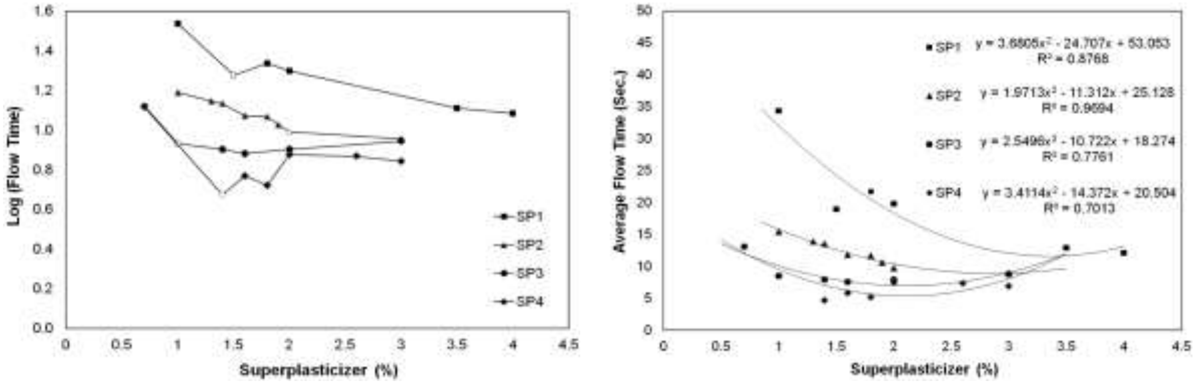

(a) (b)

Fig. 1 - (a) Marsh flow time at saturation point; and (b) flow time *vs.* dosage of superplasticizer

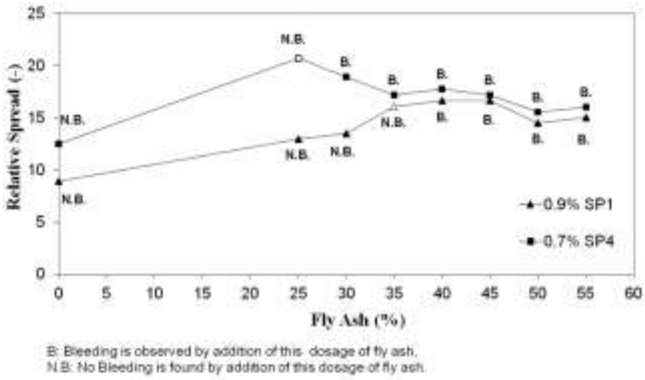

Fig. 2 - Relative spread of paste by replacing cement with different dosages of fly ash

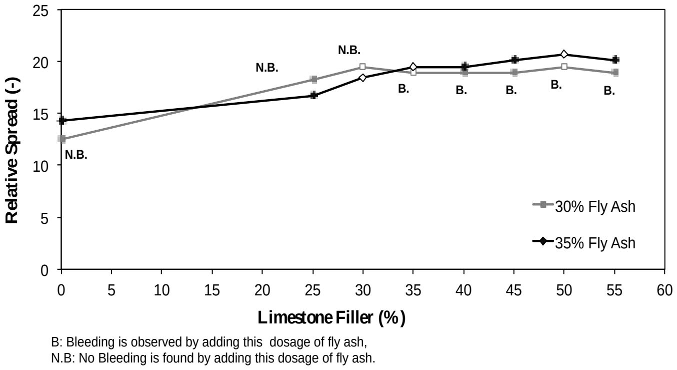

Fig. 3 - Relative spread of paste made by different percentage of limestone filler

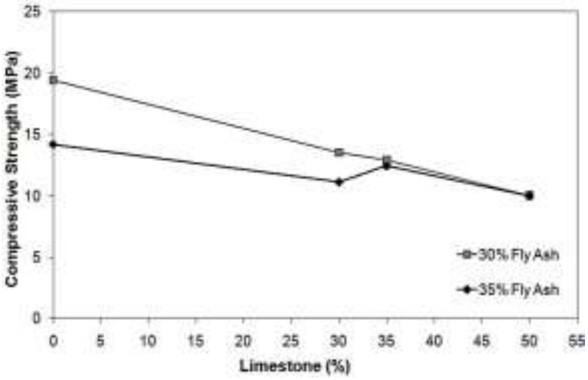

Fig. 4 - Compressive strength of mortar made of various percentages of limestone filler

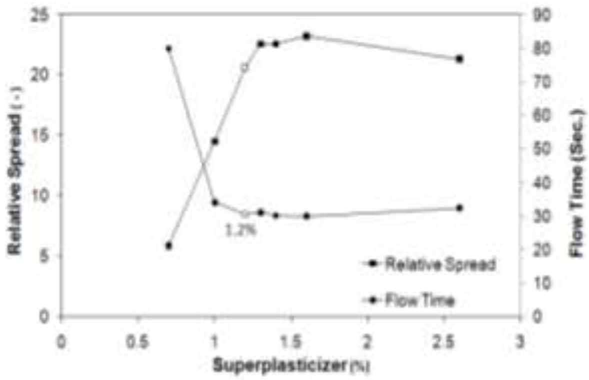

Fig. 5 - Relative spread of the paste *vs*. the percentage of superplasticizer

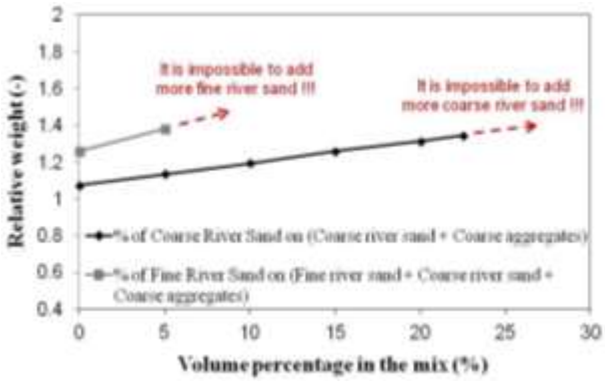

Fig. 6 - Determination of the optimum composition of the solid skeleton

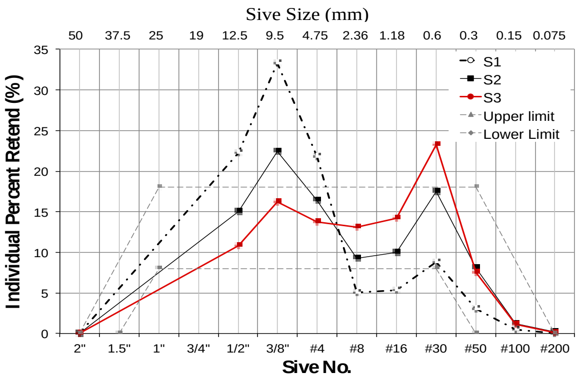

Fig. 7 - Comparison of the results with the limitation suggested by Minnesota DOT [28]

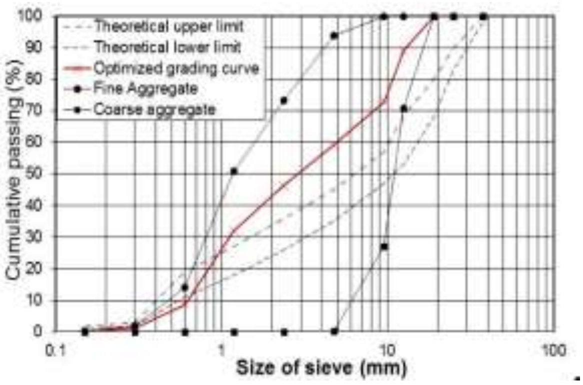

Fig. 8 - Comparison of the results with the curves defining the upper and lower limits suggested by ASTM C136 [54]for conventional concrete (fine aggregate includes the fine and coarse rive sand)

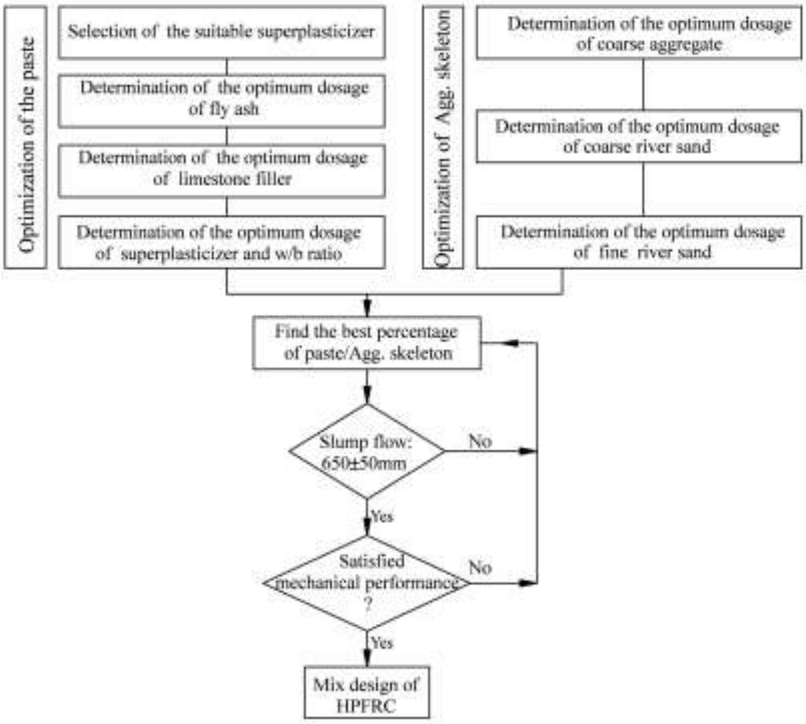

Fig. 9 - Flowchart of HPFRC mix design

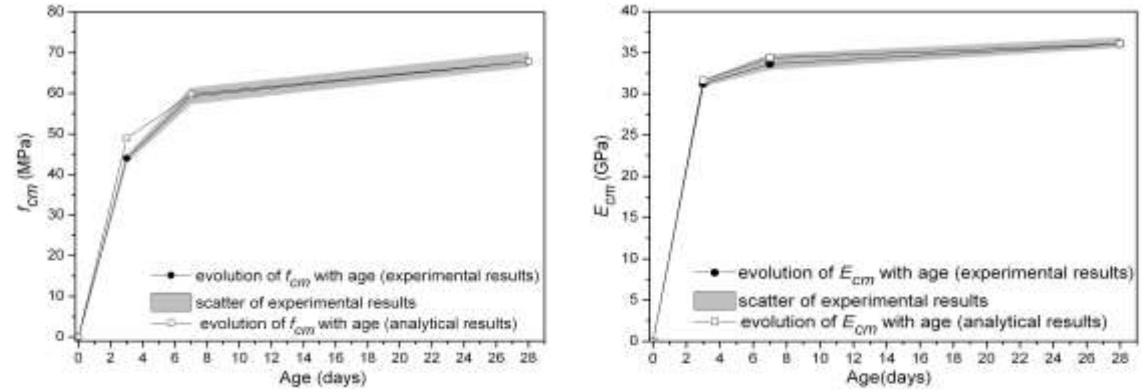

(a) (b)

Fig. 10 – Evolution with age of: (a) average compressive strength, and (b) average elasticity modulus

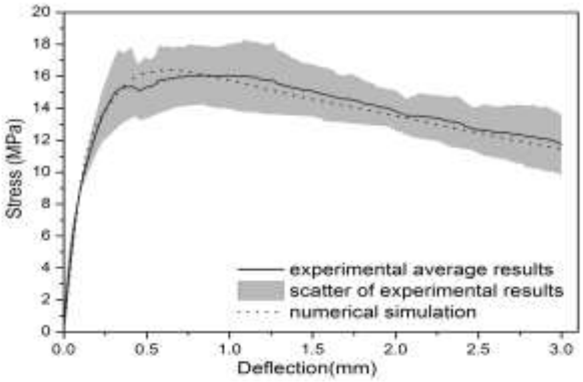

Fig. 11 – Nominal flexural stress-midspan deflection relationship

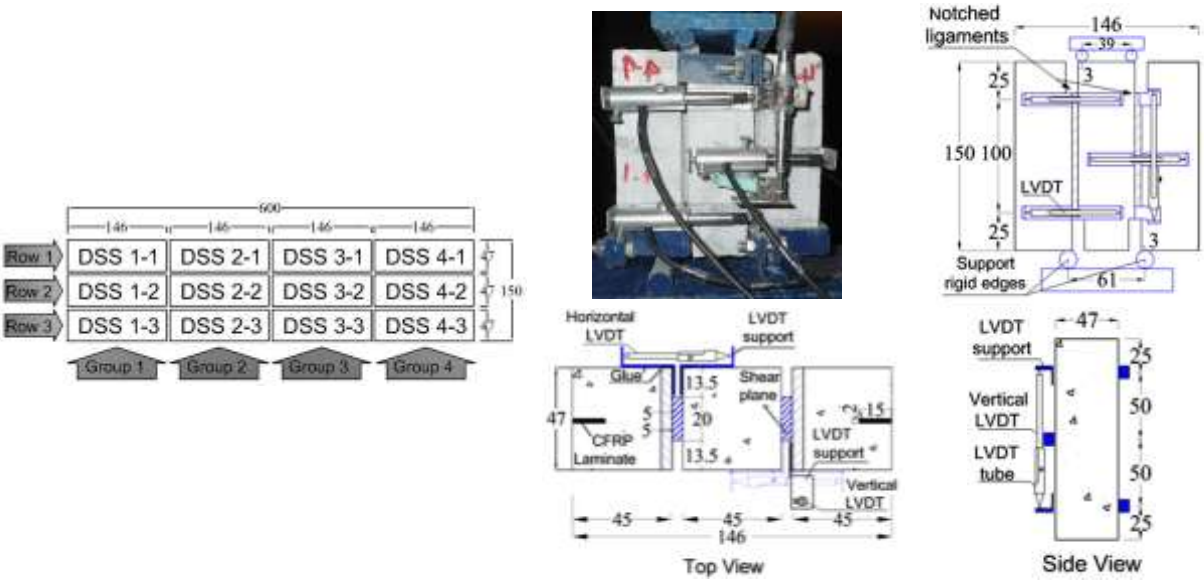

(a) (b)

Fig. 12 - (a) Location of the specimens along the prismatic element (Top view); and (b) geometry and loading configuration of DSS specimen (dimensions in mm)

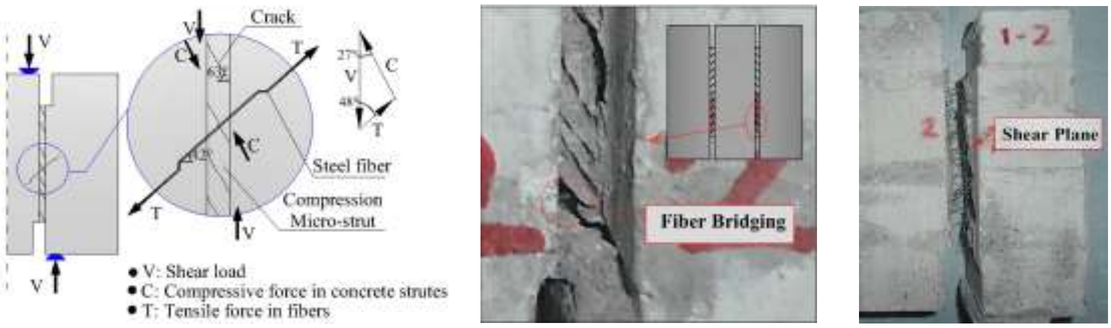

(a) (b) (c)

Fig. 13 - (a) Shear transfer during the initiation of the inclined cracks (b) formation of the crack band along the shear plane; and (c) fractured plane of the specimen

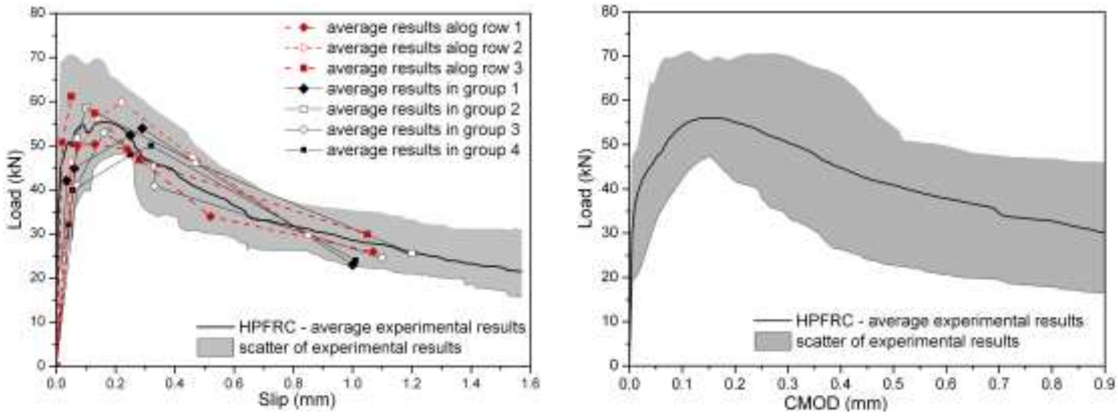

(a) (b)

Fig. 14 - Experimental results of (a) load-slip; and (b) load *vs.* CMOD relationship

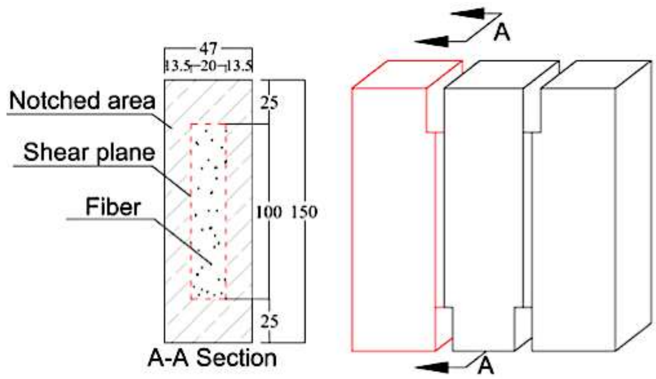

Fig. 15 - Sawn section of DSS for image analysis (dimensions in mm)

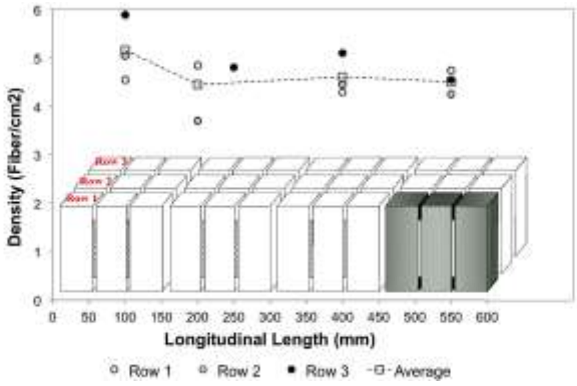

Fig. 16 - Fiber density along the beam length

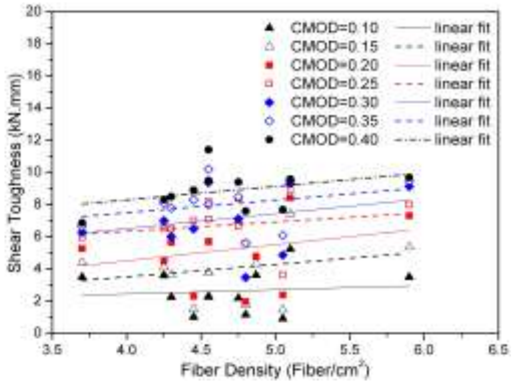

Fig. 17 - Fiber density *vs.* shear toughness of the specimens

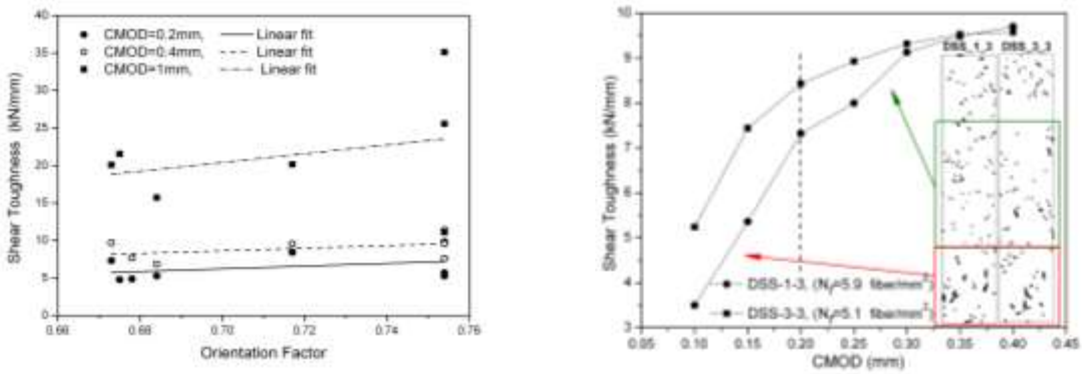

(a) (b)

Fig. 18 - (a) Fiber orientation factor *vs.* shear toughness of the specimens; and (b) Comparison of two shear plane

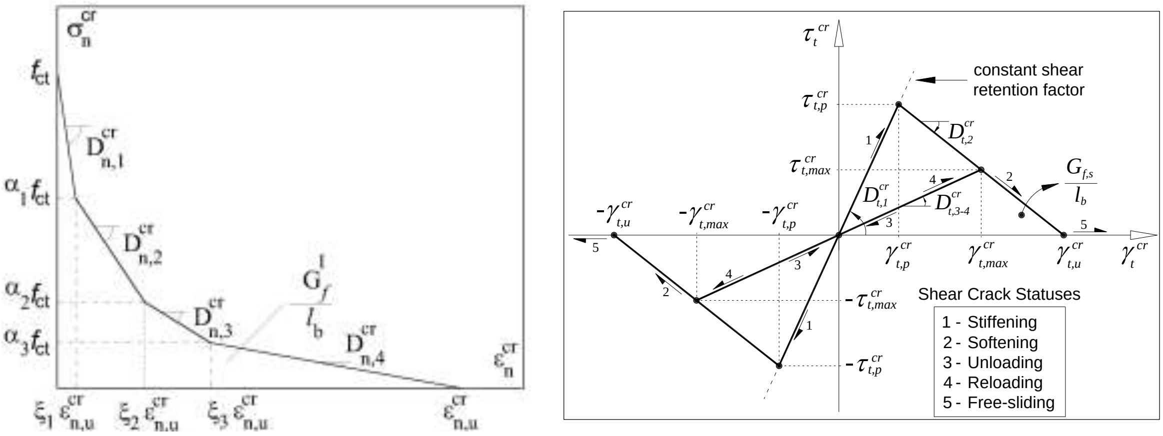

Fig. 19 - Diagrams for modeling the (a) fracture mode I ($\sigma^{cr}_{n,2} = \alpha_1\ f_{ct}$, $\sigma^{cr}_{n,3} = \alpha_2\ f_{ct}$, $\sigma^{cr}_{n,4} = \alpha_3\ f_{ct}$, $\varepsilon^{cr}_{n,2} = \xi_1\ \varepsilon^{cr}_{n,u}$, $\varepsilon^{cr}_{n,3} = \xi_2\ \varepsilon^{cr}_{n,u}$, $\varepsilon^{cr}_{n,4} = \xi_3\ \varepsilon^{cr}_{n,u}$); and (b) fracture mode II at the crack coordinate system

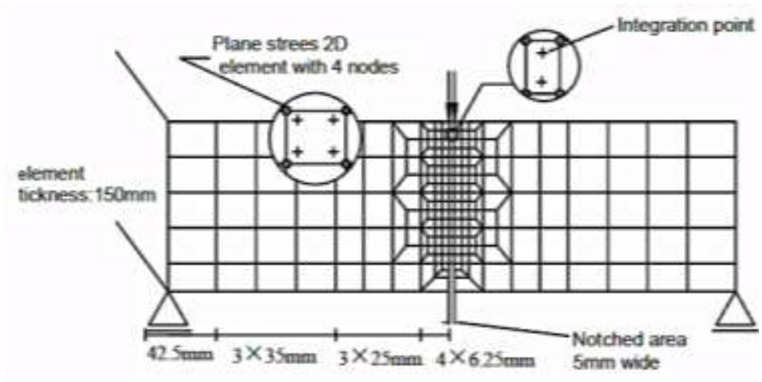

Fig. 20 - Finite element mesh relevant characteristic, load and support conditions of the type of specimen adopted in the inverse analysis

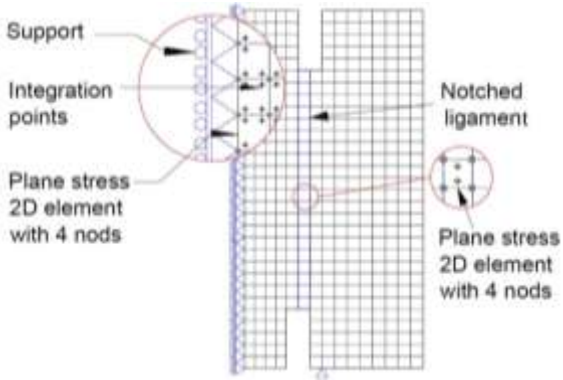

Fig. 21 - Finite element model for simulating mixed mode fracture tests

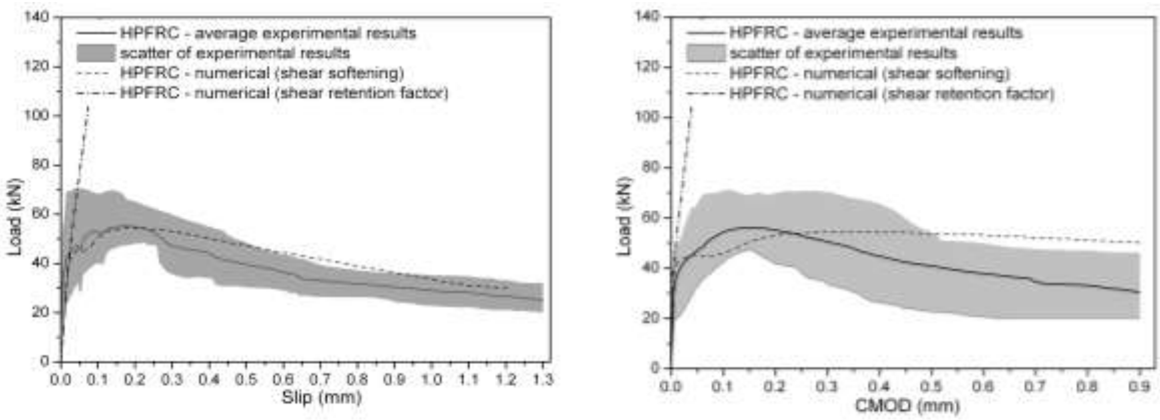

Fig. 22 - Comparison between numerical and experimental results of (a) load *vs.* slip; and (b) load *vs.* CMOD relationships

Table 1- Physical property of cement, fly ash and limestone filler

Parameter	Value	Unit
CEM I 42.5R [47, 48]		
Specific gravity	3150	Kg/m^3
Blaine fineness	387.3	m^2/Kg
Setting time (initial)	116	min
Setting time (final)	147	min
Fly Ash class F [49, 50]		
Specific gravity	2360	Kg/m^3
Blaine fineness	387.9	m^2/Kg
Particles < 75 μm	81.15-94.40	%
Particles < 45 μm	68.45-85.90	%
Limestone Filler [47, 48]		
specific gravity	2700	Kg/m^3
particles < 80 μm	92.0	%
particles < 2 μm	15.0	%
mean particle size	5.0	μm

Table 2 - Optimum paste composition

Material	**Volume % of Paste**
Cement	36.95
Fly ash	11.09
Limestone filler	11.09
Water	40.28
Superplasticizer	0.59

Table 3 - Aggregate properties

Aggregate	Specific Gravity[1] (Kg/m^3)	Absorption[1] (%)	Maximum size[2] (mm)
Fine river sand	2.609	10.64	2.36
Coarse river sand	2.630	5.08	4.75
Coarse aggregate	2.613	1.58	12.5

[1] According to ASTM C 127 and BS EN 1097-6 [51 and 52] and ASTM C 128 and BS EN 1097-6 [53 and 52] for, respectively, the coarse and fine aggregates.

[2] According to ASTM C 136 and BS 812-103.1 [54, 55].

Table 4 - Aggregate compositions and their effects on flowability of a concrete mix

Agg. Composition	Fine river sand	Coarse river sand	Coarse Agg.	Flow diameter	T_{50}	Comment
	(% of total volume of solid skeleton)			(mm)	(s)	
S1	4.85	19.10	76.05	-	-	The initial solid composition
S2	18	42	40	120	-	120mm slump loss, very harsh mix
S3	12	51	37	500	6	Good homogeneity

Table 5 - Concrete compositions executed with different paste percentages

Mix	Paste Volume (%)	C[1] Kg/m^3	FA[2] Kg/m^3	LF[3] Kg/m^3	W[4] L/m^3	SP[5] L/m^3	FS[6] Kg/m^3	RS[7] Kg/m^3	CA[8] Kg/m^3	SF[9] Kg/m^3	w/b[10] (-)	T_{50} (Sec.)	Spread Diam. mm
A	46	443	133	133	199	15	102	724	522	90	0.35	-	490
B	48	462	138	139	208	16	99	697	503	90	0.35	3.5	660
C	50	481	144	144	216	16	95	671	483	90	0.35	2	721

[1] Cement; [2] Fly Ash; [3] Limestone Filler; [4] Mixing Water; [5] Superplasticizer; [6] Fine River Sand; [7] Coarse River Sand; [8] Coarse Agg; [9] Steel Fibers; [10]Water to Binder Ratio.

Table 6 - Compressive strength and Young's modulus of HPFRC

Concrete age (day)	f_{cm} [1] (MPa)	CoV [4] of f_{cm} (%)	f_{ck} [2] (MPa)	E [3] (N/mm^2)	CoV [4] of E (%)
3	44.00	1.52	36.00	31246	1.01
7	59.24	2.76	51.24	33624	1.37
28	67.84	2.02	59.84	36056	1.26

[1] mean value of compressive strength; [2] characteristic value of compressive strength; [3] Young's modulus; [4] the CoV is related to testing of 5 specimens.

Table 7- Average limit of proportionality and residual flexural tensile strength parameters of HPFRC beams

	δ_L (mm)	$f_{fct,L}$ (MPa)	$f_{R,1}$ (MPa) $CMOD_1 = 0.5$	$f_{R,2}$ (MPa) $CMOD_2 = 1.5$	$f_{R,3}$ (MPa) $CMOD_3 = 2.5$	$f_{R,4}$ (MPa) $CMOD_4 = 3.5$
Average	0.05	8.58	15.45	15.26	13.63	12.13
CoV	1.70	23.6	12.45	10.76	11.06	15.89

Table 8 - Values of the fracture parameters defining the stress-strain softening laws

α_1	α_2	α_3	ξ_1	ξ_2	ξ_3	f_{ct} (MPa)	G_f^I (N/mm)	E (GPa)
0.78	0.89	0.57	0.028	0.058	0.36	7.3	7.2	40